Effect of the milling atmosphere on the microstructure and mechanical properties of a ODS Fe-14Cr model alloy

M. A. Auger[a]*, V. de Castro[b], T. Leguey[b], S. Lozano-Perez[a], P.A.J. Bagot[a], M.P. Moody[a], S.G. Roberts[a, c]

[a]Department of Materials. University of Oxford. OX1 3PH Oxford, UK.

[b]Departamento de Física. Universidad Carlos III de Madrid. 28911 Leganés, Spain.

[c]Culham Centre for Fusion Energy, Abingdon, Oxon, OX14 3EA, UK.

*Corresponding Author. Address: Department of Materials. University of Oxford. Parks Road. OX1 3PH Oxford, UK. Tel.: +44 (0) 1865 273682. Fax: +44 (0) 1865 273789.

e-mail address: maria.auger@materials.ox.ac.uk (M. A. Auger)

Abstract

A systematic study has been undertaken to assess how the milling atmosphere, in the processing of an ODS steel with nominal composition Fe-14Cr-0.3Y_2O_3 (wt. %), will affect the microstructure and mechanical properties of the resultant alloys. Batches of the steel were manufactured by a powder metallurgy route incorporating mechanical alloying, hot isostatic pressing, forging and heat treatment. Hydrogen or helium atmospheres were used in the mechanical alloying, with all other processing parameters remaining identical. Transmission electron microscopy (TEM) and Atom Probe Tomography (APT) show that both milling atmospheres promote a homogeneous dispersion of Y-rich nanoparticles in the final alloys, being smaller when milling in H. Previously reported mechanical characterisation of these alloys shows better mechanical response at high temperature for the alloy milled in a H. This

can be justified by the presence of smaller Y-rich nanoparticles together with the absence of bubbles, observed in the alloy milled in He.

Keywords:

ODS steels, powder metallurgy, milling atmosphere, TEM, APT

1. Introduction

It is well known that oxide dispersion strengthened (ODS) ferritic steels show improved irradiation resistance, high-temperature mechanical properties and microstructural thermal stability, relative to equivalent non dispersion strengthened steels [1-6] These outstanding features make them suitable candidates to be used as structural materials for advanced fission and fusion applications. The overall performance of these materials depends on their microstructure, in particular their grain size distribution and the oxide nanoparticle distribution; which themselves depend on composition and processing conditions [7-9]. The standard process to manufacture ODS alloys is by powder metallurgy followed by various thermomechanical treatments [10-13]. Mechanical alloying of ODS alloys is usually performed in a protective atmosphere to prevent oxidation; Ar gas has been widely used, but mechanical alloying in He or H atmospheres has been found to result in improved mechanical properties in the final consolidated material [14-16]. All of these milling atmospheres effectively prevent material oxidation during the manufacturing process, however, bubble formation was observed in the final material when Ar or He had been used in the powder milling [17, 18]. The presence of such bubbles is detrimental to the mechanical properties [3, 19] and should be avoided. On the other hand, no bubbles have been observed in consolidated ODS material when milling in H [20]. Furthermore, no deleterious hydrides formation was detected in that case.

In the present work, ODS alloys based on Fe-14Cr (wt. %) have been produced by

mechanical alloying in He or H atmospheres followed by hot isostatic pressing, and the resulting microstructures of these ODS alloys have been characterised.

2. Experimental procedure

The target composition of the manufactured alloys was Fe-14Cr-0.3Y_2O_3 (wt. %). Elemental Fe (99.7% pure) and Cr (99.8% pure) powders were supplied by Alfa – Aesar; powder particle sizes were < 10 μm and < 5 μm, respectively. They were blended with nanosized Y_2O_3 powder supplied by Nanophase Technologies (99.5% pure, particle size < 50 nm). The powder blends were mechanically alloyed in a Fritsch Pulverisette 6 planetary ball mill at 300 rpm and ball-to-powder ratio = 10:1 for 60 h, under pure He or H atmospheres. The milling atmosphere was the only difference between the processed alloys, keeping all other processing parameters identical. The alloyed powders were canned in 304 stainless steel cans (42 mm diam. × 57 mm height), degassed at 550^{o}C in vacuum ($p < 10^{-3}$ mbar) for 24 h and vacuum sealed. The canned powder batches were consolidated by hot isostatic pressing at 1100^{o}C and 200 MPa for 2 h. The consolidated billets were forged at 1100^{o}C, obtaining ~ 12 mm × 12 mm × 170 mm bars, which were finally heat treated at 850^{o}C for 2 h. To simplify the nomenclature in the subsequent presentation and discussion of results, the alloys will be referred to as 14YET and 14YHT, corresponding to He and H milling atmospheres, respectively.

The microstructure of these materials was investigated by transmission electron microscopy (TEM) and Atom Probe Tomography (APT). 3 mm disks were extracted from the bulk materials to prepare TEM samples. A TENUPOL 5 twin-jet polisher with a solution of 5% vol. perchloric acid + 95 % vol. methanol at – 40^{o}C, typical for ferritic-martensitic and ODS steels sample preparation [21, 22], was used for electropolishing. Additional cleaning for 5 min in a plasma cleaner was applied prior to each TEM session. Bright field TEM images and

microdiffraction patterns were obtained in a JEOL 3000F microscope operated at 300 keV. Energy-filtered TEM (EFTEM) maps were obtained with a JEOL 2200MCO prototype microscope equipped with two spherical aberration (Cs) correctors and a Ω filter. EFTEM Y maps were acquired in the low loss region using the $N_{2,3}$ edge (onset at 26 eV). The EFTEM data were processed after acquisition using multivariate statistical analysis (MSA) [22].

Atom Probe Tomography samples were cut from the bulk materials in rod shape ~ 0.5 × 0.5 × 20 mm and then subjected to a conventional two steps electropolishing process [23]. First, a rough polishing was performed by a double-layer method in which the specimen is repeatedly dipped into a layer of electrolyte (25% vol. perchloric acid, 75% vol. acetic acid) on top of an inert liquid (Galden^{TM} solution, perfluorinated polyether PFPE) applying a DC voltage of 15 V which was reduced to 10 V as the specimen area reduced to a circular necked region and then split into 2 parts. Each of these parts was subjected to a micropolishing process in which the specimen is repeatedly pushed through a gold loop that holds a drop of electrolyte (2% vol. perchloric acid, 98 % vol. 2-butoxyethanol). A DC voltage of 8 to 5 V is applied until the specimen's end is suitable for atom probe analysis, i. e. having a radius of curvature at the apex around or below 100 nm .

The APT analysis was carried out in a CAMECA Instruments LEAP® 3000X-HR operating in laser pulsing mode. An APT specimen base temperature of 30 or 50 K was used with a laser energy of 0.3 – 0.4 nJ at a repetition rate of 200 kHz. Data sets containing 20 – 25 million of ions were obtained, and data were reconstructed and analysed using IVAS 3.6.6 commercial software [24].

3. Results and discussion

3.1. Microstructural characterisation

3.1.1. TEM analysis

Fig. 1-a) shows the microstructure of the 14YET alloy. Nanoparticles are distributed mostly within grains, and also pinning grain boundaries and dislocations. Particle diameters are all less than 30 nm, with most of the particles less than 10 nm in diameter. The number density of visible particles was quantified in three regions; values found were: 0.10 ± 0.02, 1.0 ± 0.2 and 1.5 ± 0.3 ($\times 10^{23}$ m^{-3}).

An EFTEM Y $N_{2,3}$ map from the same region displayed in Fig 1-a) can be seen in Fig. 1-b), demonstrating that the nanoparticles are Y-rich. A detailed TEM study of this same alloy can be found in [18] and [25], in which a Y-O rich core and a Cr rich shell structure was found to be present in the majority of the particles, at least for the studied regions. Nanovoids of ~ 5 nm size, which might contain gas atoms derived from the milling atmosphere, were found in this alloy [18]. These nanovoids are not apparent in Fig. 1 as, due to their small size, they are only viewed out of focus. In the regions of study, most voids are found next to the particles.

The microstructure of the 14YHT alloy is shown in Fig. 2-a). A fine dispersion of nanoprecipitates is found inside grains. All particles are below 30 nm in diameter, with mean diameter = 8 ± 6 nm. The number density of visible particles was determined in three regions; values found were 0.12 ± 0.02, 4.7 ± 0.9 and 9 ± 2 ($\times 10^{22}$ m^{-3}). The EFTEM analysis shown in Fig. 2-b) shows that the nanoparticles are Y-rich. Additional TEM observation of this same alloy is described in [20]. Fig. 3 shows HRTEM images of several of the nanoparticles found in the 14YHT sample. The particle displayed in Fig.3-a) was indexed as orthorhombic $YCrO_3$ viewed down zone axis [011]. The particle displayed in Fig.3-c) was indexed as body-centred cubic (bcc) Y_2O_3 viewed down zone axis [112]. These TEM observations did not identify the presence of nanovoids in this material; though, positron annihilation spectroscopy has revealed the presence of vacancy type defects in this same alloy [26, 27].

3.1.2. APT analysis

The mass spectra obtained by APT for the 14YET and 14YHT alloys was almost identical for both materials and produced a very similar respective measurements of the overall bulk composition. These results are displayed in Table I together with the nominal composition values. Ion maps for 14YET and 14YHT are displayed in Figs. 4 and 5, respectively. Both samples show a homogeneous distribution of Cr in the iron matrix, while Y, Y-O and Cr-O ions appear clustered and evenly distributed within the analysed volume.

A cluster analysis based on the maximum separation method [28] was applied to define clusters. This method assumes that the distance between two solute ions (Y, Y-O and Cr-O in this case) within a cluster is smaller than the distance between two solute ions found elsewhere in the reconstructed volume. Hence, in this approach, all pairs of solute ions with a separation less than the user-defined distance d_{max} are assigned to be in the same cluster. To avoid the inclusion of random clusters, i.e. clusters occurring by statistical fluctuations in a nominally homogeneous distribution of solute in the analysis, a minimum number of ions in the cluster, N_{min}, is imposed. This N_{min} parameter filters the analysed data by removing all clusters consisting of less than N_{min} atoms. The cluster selection parameters for each alloy were optimised for detection of clusters according to the criteria developed in [29]: d_{max} = 1.6 nm and N_{min} =7 were used to analyse data from the 14YET alloy; d_{max} = 1.3 nm, N_{min} =12 for 14YHT. 265 and 236 clusters were found, respectively, in the analysed volumes of 14YET and 14YHT.

The cluster size was calculated in terms of the Guinier diameter, i.e. twice the Guinier radius [30]. Figs. 6-a) and b) show the cluster size histograms obtained for the 14YET and 14YHT alloys, respectively. Table II presents a summary of the statistical analysis of the measured cluster size, number density and volume fraction for each alloy. It can be seen that there is less dispersion in particle size for the 14YHT than for the 14YET alloy. The mean particle size for 14YHT is 4% smaller than for 14YET; also, the experimental error is 35% smaller in

14YHT than in 14YET. In agreement with TEM observations, the number density of clusters in the 14YET alloy was higher than in the 14YHT alloy.

Best-fit ellipsoids were used to define the shape of the clusters. The smallest, middle and largest characteristic lengths of the best-fit ellipsoids can be used to calculate the oblateness (smallest characteristic length / middle characteristic length) and the aspect ratio (middle characteristic length / largest characteristic length) of the clusters. Oblateness and aspect ratio measurements for each cluster for both alloys are shown in Fig. 7; this figure also indicate how the combination of oblateness and aspect ratio can be used to define the cluster shape as sphere, rod, lath or disc [31]. In both alloys, most of the clusters tend towards a spherical shape, but this tendency is somewhat more pronounced in the 14YHT alloy than in 14YET. (Table III).

The chemical composition of the clusters was also analysed by APT. Figs. 8-a) and 8-b) show the Y, O and Cr content in the clusters vs their Guinier diameter for 14YET and 14YHT, respectively. Y and O content, or Y/O ratio, tends to be random for the smallest clusters found in both alloys, but compositions stabilize above a threshold size. In 14YET (Fig. 8-c)), Y/O ratio = 1.17 ± 0.12 for Guinier diameter larger than 4.08 nm and, in 14YHT (Fig. 8-d), Y/O ratio = 1.04 ± 0.10 for Guinier diameter larger than 3.82 nm.

Cr was not always present in the clusters. In the 14YET sample, 52 out of 265, i. e. 20% of the clusters characterised in the analysed volume, did not contain Cr. The Cr content in the other clusters was between 0.4 and 8.3 at. %. In the 14YHT sample, 24 out of 231 clusters (10% of them) did not contain Cr. The Cr content in the other clusters was between 0.5 and 7.4 at. %. No correlation between the Cr content and the cluster size could be established in this case (Figs. 8-a) and b)).

Cr-O ions appear to surround the clusters rather than being incorporated in the core. In both alloys, most of the Y rich clusters were enclosed by Cr-O isoconcentration surfaces

(isosurfaces); an example of this can be seen in Fig. 9. The isoconcentration surface values for Cr-O (0.3 at. %) and Y ions (1.0 at. %) displayed in Fig. 9 were selected as those visually enclosing the majority of the perceptible clusters in the 3D reconstructed volume. Cr-O isosurfaces were usually irregular in the 14YET sample (Fig. 9-a), but they generally replicated the Y-rich cluster shape in the 14YHT alloy (Fig. 9-b).

3.2. Mechanical properties

The mechanical properties of the 14YET and 14YHT have been reported in [10] and [20], respectively. In those studies, tensile tests were performed on flat tensile specimens (20 mm gauge length × 3 mm width × 1 mm thickness) at a constant crosshead rate of 0.1 mm/min at 25, 400, 500, 600 and 700^{o}C. A flow of pure Ar was supplied while testing above room temperature in order to prevent surface oxidation.

Fig. 10 displays the stress-strain curves of both alloys at different test temperatures, from room temperature up to 700^{o}C. Table IV summarizes the mechanical properties (yield strength, ultimate tensile strength, uniform elongation and total elongation) in that temperature range. Both alloys show a similar tendency vs. temperature. Individual yield-strength values for 14YHT are lower than 14YET at room temperature and at 600^{o}C, almost the same at 400^{o}C and higher than 14YET at 500 and 700^{o}C. The yield strength value at the highest tested temperature, 700^{o}C, in the 14YHT alloy is 25% higher than in the 14YET alloy.

As described in section 3.1.1, nanovoids of ~ 5 nm diameter were observed by TEM in the 14YET alloy; these might contain gas atoms derived from the milling atmosphere. Such nanovoids might coarsen with temperature according to the observations made in [32], in which bubbles present in a nanostructured ferritic alloy coarsen following thermal treatment at a temperature of 750^{o}C for 10 h and 100 h. This might account for the decrease in strength

in this alloy type with increasing temperature.

No nanovoids were observed by TEM in the 14YHT, but positron annihilation analysis revealed the presence of vacancy type defects in this alloy, which were stable at temperatures up to 750^{o}C [26]. The stability of these defects even at high temperature, together with the presence of a higher density of smaller nanoparticles in the 14YHT alloy might account for its better mechanical performance at high temperature.

4. Conclusions

In this work, two alloys with nominal composition Fe-14Cr-0.3Y_2O_3 (wt. %) have been produced by a powder metallurgy route consisting in: mechanical alloying of Fe and Cr elemental powders with nanometric Y_2O_3 powder in pure He and H atmospheres, canning and degassing, hot isostatic pressing, forging and heat treatment. The microstructure and mechanical properties of the obtained alloys have been characterised. The following conclusions were realised:

- Complementary TEM and APT revealed the presence of Y rich nanoparticles, mostly inside grains in both alloys but, in the 14YET alloy they were also pinning grain boundaries and dislocations. From APT, the mean cluster size and its standard deviation were found to be smaller in the 14YHT than in the 14YET alloy.
- TEM and APT both demonstrate the cluster number density to be higher in the 14YET alloy than in 14YHT.
- The shape of the clusters is mainly spherical, but a higher fraction of spherical nanoparticles was found in the 14YHT alloy by APT.
- TEM and APT both found the nanoparticles to mainly contain Y and O; Cr was found in some, but not in all of them.
- Cr-O rich isosurfaces could be defined surrounding most of the clusters in both alloys

by APT. The shape of these isosurfaces replicated the geometry of the Y-rich nanoclusters in the 14YHT alloy, but they displayed more irregular shapes in the 14YET alloy.

- The yield strength value at 700^{o}C, the highest tested temperature in this study, is higher for the 14YHT alloy. It can be due to the presence of nanovoids observed by TEM in the 14YET alloy, which might coarsen with temperature. The presence of smaller nanoparticles in the 14YHT might also contribute to this better mechanical performance.

Acknowledgements

This work was supported by Ministerio de Economía y Competitividad (Contract ENE2012-39787-C6-05), Comunidad de Madrid through the program MULTIMAT (S2013/MIT-2862), the European Commission through the European Fusion Development Agreement, the FP7-EU Program under Grant Agreement 312483 – ESTEEM2 (Integrated Infrastructure Initiative-I3), EPSRC Grant Number EP/H018921/1 and The Royal Society (2011/R1 International Exchanges Application)

References

[1] S. Ukai, M. Harada, H. Okada, M. Inoue, S. Nomura, S. Shikakura, K. Asabe, T. Nishida, M. Fujiwara, Alloying Design of Oxide Dispersion-Strengthened Ferritic Steel for Long-Life Fbrs Core Materials, J Nucl Mater 204 (1993) 65-73.
[2] D.T. Hoelzer, J. Bentley, M.A. Sokolov, M.K. Miller, G.R. Odette, M.J. Alinger, Influence of particle dispersions on the high-temperature strength of ferritic alloys, J Nucl Mater 367 (2007) 166-172.
[3] G.R. Odette, M.J. Alinger, B.D. Wirth, Recent developments in irradiation-resistant steels, Annu Rev Mater Res 38 (2008) 471-503.
[4] A. Hirata, T. Fujita, Y.R. Wen, J.H. Schneibel, C.T. Liu, M.W. Chen, Atomic structure of nanoclusters in oxide-dispersion-strengthened steels, Nat Mater 10 (2011) 922-926.
[5] J.H. Kim, T.S. Byun, J.H. Lee, J.Y. Min, S.W. Kim, C.H. Park, B.H. Lee, Effects of processing condition on the microstructural and tensile properties of 14Cr-based oxide dispersion strengthened alloys, J Nucl Mater 449 (2014) 300-307.
[6] C. Burrows, The irradiation resistance of oxide dispersion strengthened steels, in: d.g.i. University of Oxford (Ed.), Thesis (D.Phil.)--University of Oxford, 2015., 2014.
[7] M.J. Alinger, G.R. Odette, D.T. Hoelzer, On the role of alloy composition and processing parameters in nanocluster formation and dispersion strengthening in nanostuctured ferritic alloys, Acta Mater 57 (2009) 392-406.

[8] N. Baluc, J.L. Boutard, S.L. Dudarev, M. Rieth, J.B. Correia, B. Fournier, J. Henry, F. Legendre, T. Leguey, M. Lewandowska, R. Lindau, E. Marquis, A. Munoz, B. Radiguet, Z. Oksiuta, Review on the EFDA work programme on nano-structured ODS RAF steels, J Nucl Mater 417 (2011) 149-153.
[9] M.J. Gorley, Powder processing of oxide dispersion strengthened alloys for nuclear applications, University of Oxford, Thesis (D.Phil.), 2014.
[10] M.A. Auger, T. Leguey, A. Munoz, M.A. Monge, V. de Castro, P. Fernandez, G. Garces, R. Pareja, Microstructure and mechanical properties of ultrafine-grained Fe-14Cr and ODS Fe-14Cr model alloys, J Nucl Mater 417 (2011) 213-216.
[11] M.A. Auger, V. de Castro, T. Leguey, A. Munoz, R. Pareja, Microstructure and mechanical behavior of ODS and non-ODS Fe-14Cr model alloys produced by spark plasma sintering, J Nucl Mater 436 (2013) 68-75.
[12] Z. Oksiuta, P. Hosemann, S.C. Vogel, N. Baluc, Microstructure examination of Fe-14Cr ODS ferritic steels produced through different processing routes, J Nucl Mater 451 (2014) 320-327.
[13] H.T. Zhang, Y.N. Huang, H.P. Ning, C.A. Williams, A.J. London, K. Dawson, Z.L. Hong, M.J. Gorley, C.R.M. Grovenor, G.J. Tatlock, S.G. Roberts, M.J. Reece, H.X. Yan, P.S. Grant, Processing and microstructure characterisation of oxide dispersion strengthened Fe-14Cr-0.4Ti-0.25Y(2)O(3) ferritic steels fabricated by spark plasma sintering, J Nucl Mater 464 (2015) 61-68.
[14] Z. Oksiuta, N. Baluc, Effect of mechanical alloying atmosphere on the microstructure and Charpy impact properties of an ODS ferritic steel, J Nucl Mater 386-88 (2009) 426-429.
[15] N.Y. Iwata, T. Liu, P. Dou, R. Kasada, A. Kimura, T. Okuda, M. Inoue, F. Abe, S. Ukai, S. Ohnuki, T. Fujisawa, Effects of MA environment on the mechanical and microstructural properties of ODS ferritic steels, J Nucl Mater 417 (2011) 162-165.
[16] S. Noh, B.K. Choi, S.H. Kang, T.K. Kim, Influence of mechanical alloying atmospheres on the microstructures and mechanical properties of 15Cr ODS steels, Nucl Eng Technol 46 (2014) 857-862.
[17] M. Klimiankou, R. Lindau, A. Moslang, Energy-filtered TEM imaging and EELS study of ODS particles and argon-filled cavities in ferritic-martensitic steels, Micron 36 (2005) 1-8.
[18] V. de Castro, T. Leguey, M.A. Auger, S. Lozano-Perez, M.L. Jenkins, Analytical characterization of secondary phases and void distributions in an ultrafine-grained ODS Fe-14Cr model alloy, J Nucl Mater 417 (2011) 217-220.
[19] P.D. Edmondson, C.M. Parish, Y. Zhang, A. Hallen, M.K. Miller, Helium bubble distributions in a nanostructured ferritic alloy, J Nucl Mater 434 (2013) 210-216.
[20] M.A. Auger, V. de Castro, T. Leguey, M.A. Monge, A. Munoz, R. Pareja, Microstructure and tensile properties of oxide dispersion strengthened Fe-14Cr-0.3Y(2)O(3) and Fe-14Cr-2W-0.3Ti-0.3Y(2)O(3), J Nucl Mater 442 (2013) S142-S147.
[21] M.M. Li, L.Y. Wang, J.D. Almer, Dislocation evolution during tensile deformation in ferritic-martensitic steels revealed by high-energy X-rays, Acta Mater 76 (2014) 381-393.
[22] S. Lozano-Perez, V. de Castro, R.J. Nicholls, Achieving sub-nanometre particle mapping with energy-filtered TEM, Ultramicroscopy 109 (2009) 1217-1228.
[23] B. Gault, Atom Probe Microscopy, Springer, New York, 2012.
[24] IVAS 3.6.6 © 2013 CAMECA Instruments, Inc.
[25] V. de Castro, S. Lozano-Perez, E.A. Marquis, M.A. Auger, T. Leguey, R. Pareja, Analytical characterisation of oxide dispersion strengthened steels for fusion reactors, Mater Sci Tech-Lond 27 (2011) 719-723.
[26] R. Dominguez-Reyes, M.A. Auger, M.A. Monge, R. Pareja, Positron annihilation study of the vacancy clusters in ODS Fe-14Cr alloys, Philos Mag (2016) Submitted.
[27] P. Parente, T. Leguey, V. de Castro, T. Gigl, M. Reiner, C. Hugenschmidt, R. Pareja, Characterization of ion-irradiated ODS Fe-Cr alloys by doppler broadening spectroscopy using a positron beam, J Nucl Mater 464 (2015) 140-146.
[28] M.K. Miller, Atom probe tomography : analysis at the atomic level, Kluwer Academic/Plenum Publishers, New York ; London, 2000.
[29] C.A. Williams, D. Haley, E.A. Marquis, G.D.W. Smith, M.P. Moody, Defining clusters in APT reconstructions of ODS steels, Ultramicroscopy 132 (2013) 271-278.
[30] M.K. Miller, E.A. Kenik, Atom probe tomography: A technique for nanoscale characterization, Microsc Microanal 10 (2004) 336-341.
[31] R.K.W. Marceau, L.T. Stephenson, C.R. Hutchinson, S.P. Ringer, Quantitative atom probe analysis of nanostructure containing clusters and precipitates with multiple length scales, Ultramicroscopy 111 (2011) 738-742.
[32] P.D. Edmondson, C.M. Parish, Q. Li, M.K. Miller, Thermal stability of nanoscale helium bubbles in a 14YWT nanostructured ferritic alloy, J Nucl Mater 445 (2014) 84-90.

Table captions

Table I. 14YET and 14YHT average chemical composition in bulk from APT analysis together with the nominal composition.

Table II. Cluster size summary, number density of clusters and volume fraction of clusters in the 14YET and 14YHT alloys.

Table III. Cluster shape summary for 14YET and 14YHT alloys.

Table IV. Mechanical properties summary for 14YET and 14YHT alloys, from [10] and [20].

Figure captions

Fig. 1 TEM images of the 14YET alloy. a) Elastic image; nanoparticles are visible although their contrast is low. b) EFTEM Y $N_{2,3}$ map of the same area; regions of high Y density correspond to the nanoparticles seen in a).

Fig. 2 TEM images of the 14YHT alloy. a) Elastic image; nanoparticles are visible although their contrast is low. b) EFTEM Y $N_{2,3}$ map of the same area, clearly showing the Y-rich nanoparticles within grains and pinning grain boundaries.

Fig. 3. HRTEM images from the 14YHT alloy. a) bright field image of particle indexed as $YCrO_3$ in zone axis [011], b) FFT diffractogram from a). c) bright field image of particle indexed as bcc Y_2O_3 in zone axis [112], d) FFT diffractogram from c).

Fig. 4. 3D ion maps from atom probe analysis reconstruction for the 14YET alloy: a) Cr ions (Video 1). b) Cr-O ions (Video 2). c) Y ions (Video 3). d) Y-O ions (Video 4).

Fig. 5. 3D ion maps from atom probe analysis reconstruction for the 14YHT alloy a) Cr ions (Video 5). b) Cr-O ions (Video 6). c) Y ions (Video 7). d) Y-O ions (Video 8).

Fig. 6. Cluster size (Guinier diameter) distribution for a) 14YET and b) 14YHT

Fig. 7. Cluster morphology analysis for a) 14YET and b) 14YHT

Fig. 8. Y, Cr and O ionic content in the clusters as a function of the cluster size for a) 14YET and b) 14YHT. Y/O ratio as a function of the cluster size for c) 14YET and d) 14YHT.

Fig. 9. 0.3 at. % Cr-O isosurfaces surrounding 1 at. % Y isosurfaces in a) the 14YET alloy (Video 9) and b) the 14YHT alloy (Video 10). Zoomed in views from individual features in each volume are also displayed.

Fig. 10. Stress-strain curves for a) 14YET and b) 14YHT at different temperatures: room temperature (25^{o}C), 400^{o}C, 500^{o}C, 600^{o}C and 700^{o}C.

Video captions

Video 1. 3D view of Cr ions in the atom probe analysis reconstruction for the 14YET alloy.

Video 2. 3D view of Cr-O ions in the atom probe analysis reconstruction for the 14YET alloy.

Video 3. 3D view of Y ions in the atom probe analysis reconstruction for the 14YET alloy.

Video 4. 3D view of Y-O ions in the atom probe analysis reconstruction for the 14YET alloy.

Video 5. 3D view of Cr ions in the atom probe analysis reconstruction for the 14YHT alloy.

Video 6. 3D view of Cr-O ions in the atom probe analysis reconstruction for the 14YHT alloy.

Video 7. 3D view of Y ions in the atom probe analysis reconstruction for the 14YHT alloy.

Video 8. 3D view of Y-O ions in the atom probe analysis reconstruction for the 14YHT alloy.

Video 9. 3D view of TEM images of 0.3 at. % Cr-O isosurfaces surrounding 1 at. % Y isosurfaces in the 14YET alloy.

Video 10. 3D view of TEM images of 0.3 at. % Cr-O isosurfaces surrounding 1 at. % Y isosurfaces in the 14YHT alloy.

Figure_1
Click here to download high resolution image

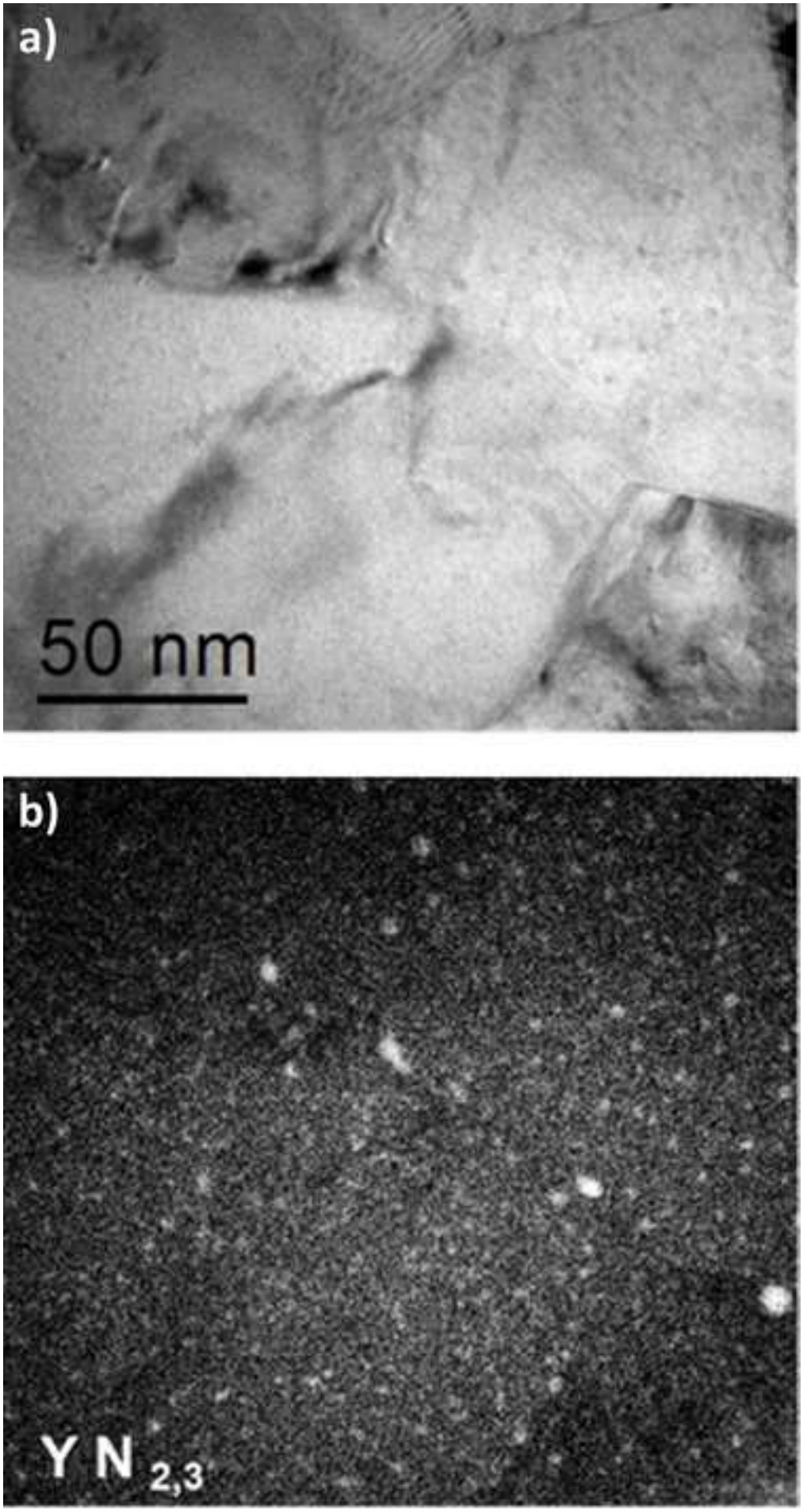

Figure_2
Click here to download high resolution image

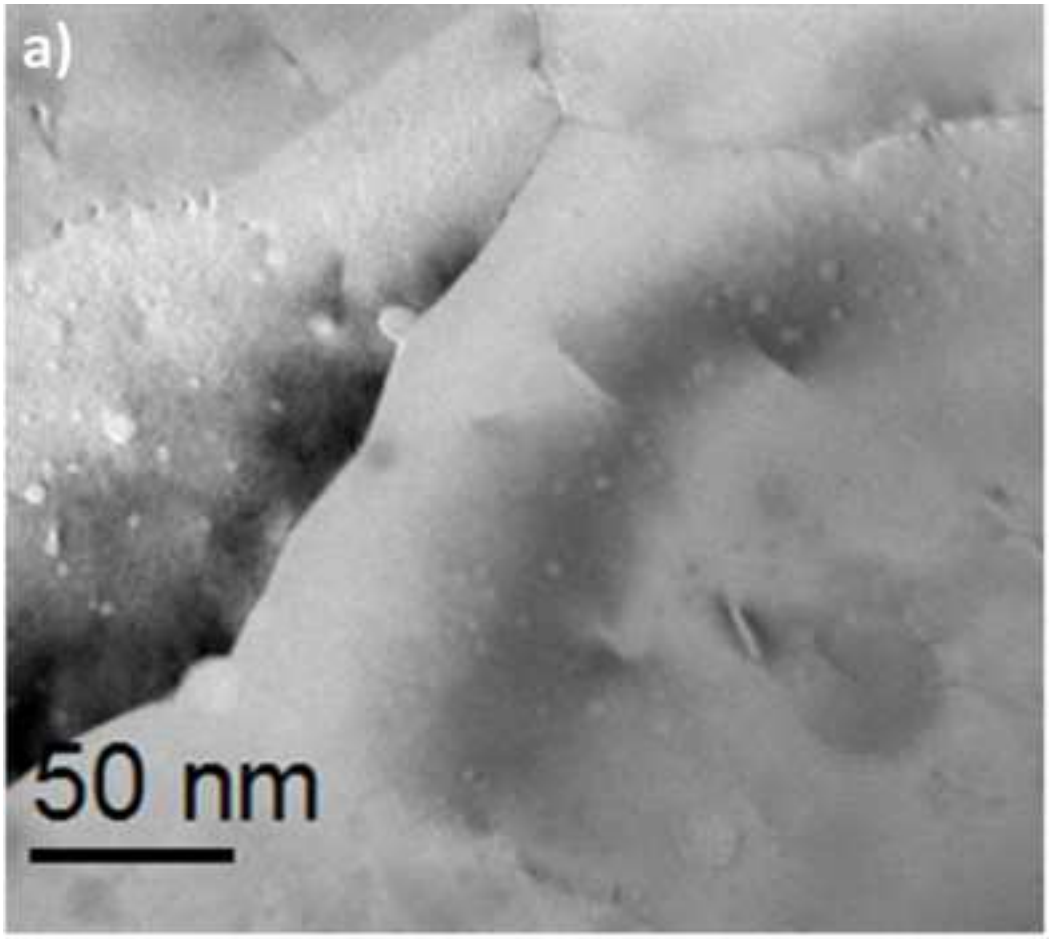

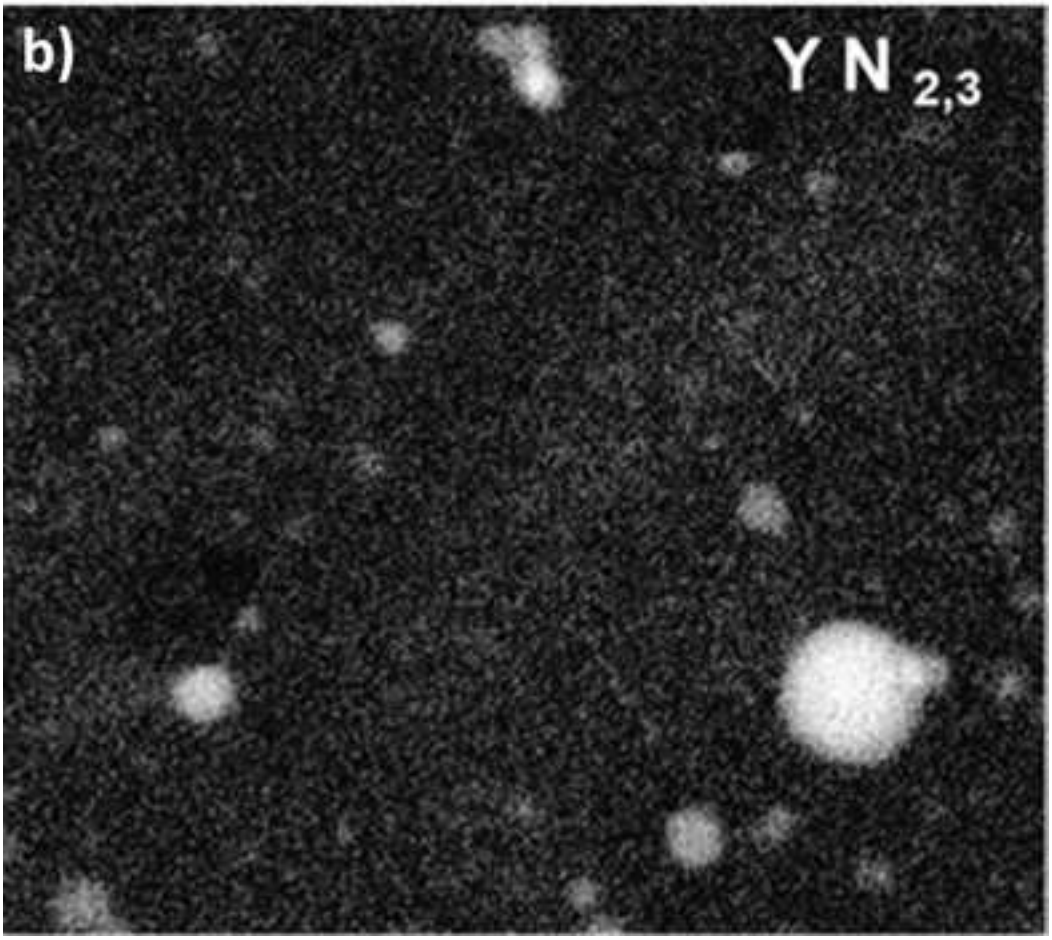

Figure_3
Click here to download high resolution image

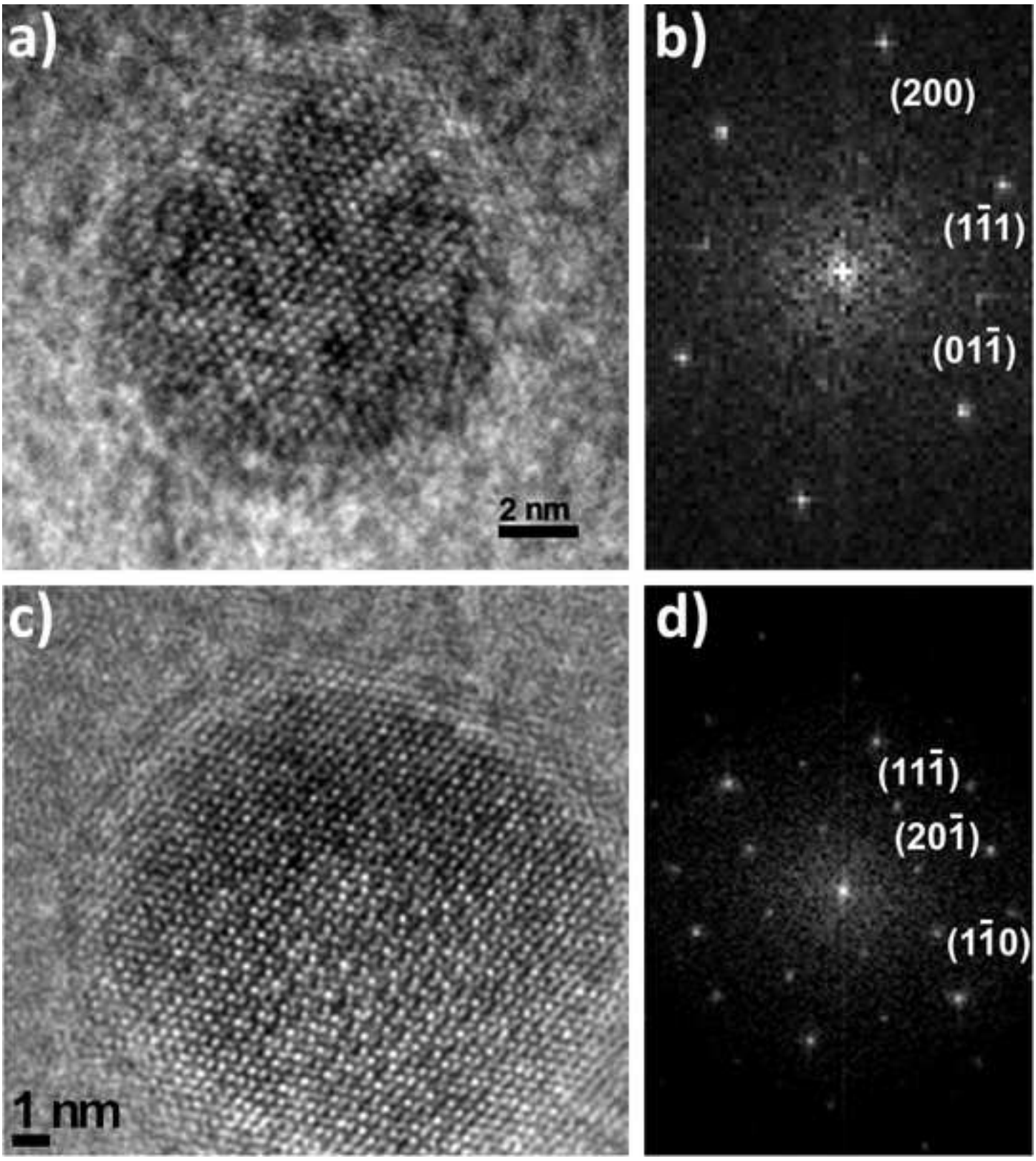

Figure_4
Click here to download high resolution image

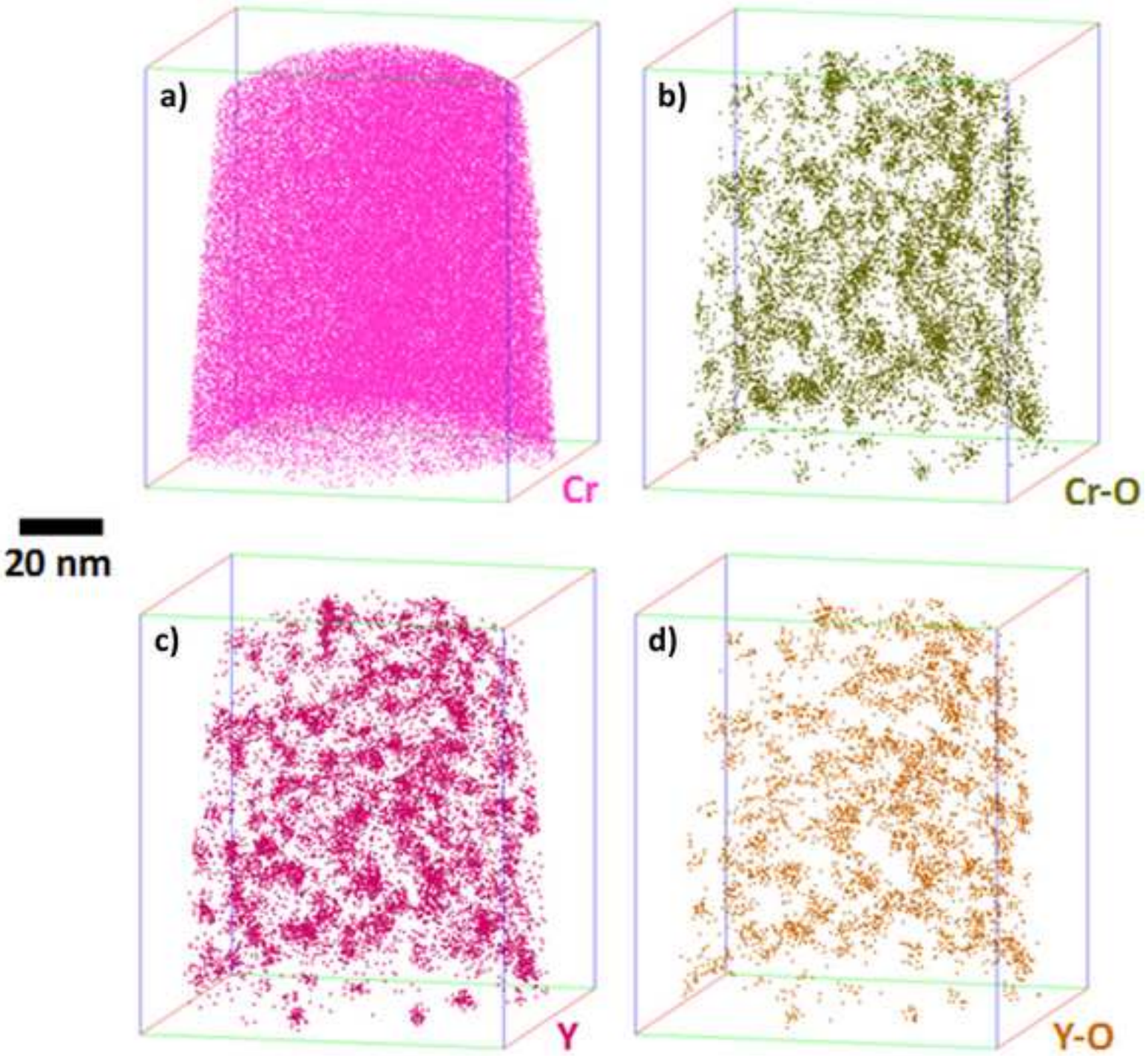

Figure_5
Click here to download high resolution image

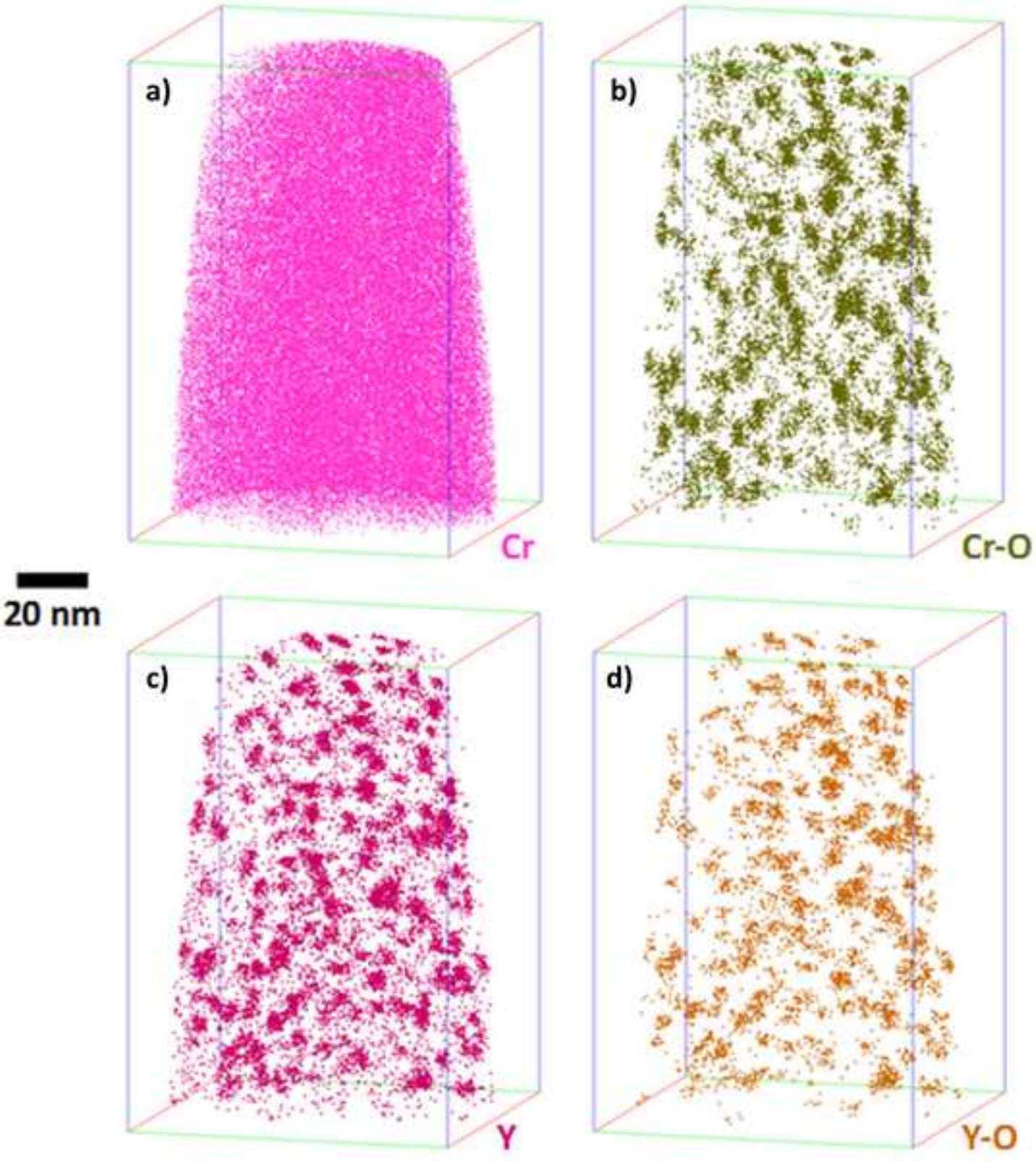

Figure_6
Click here to download high resolution image

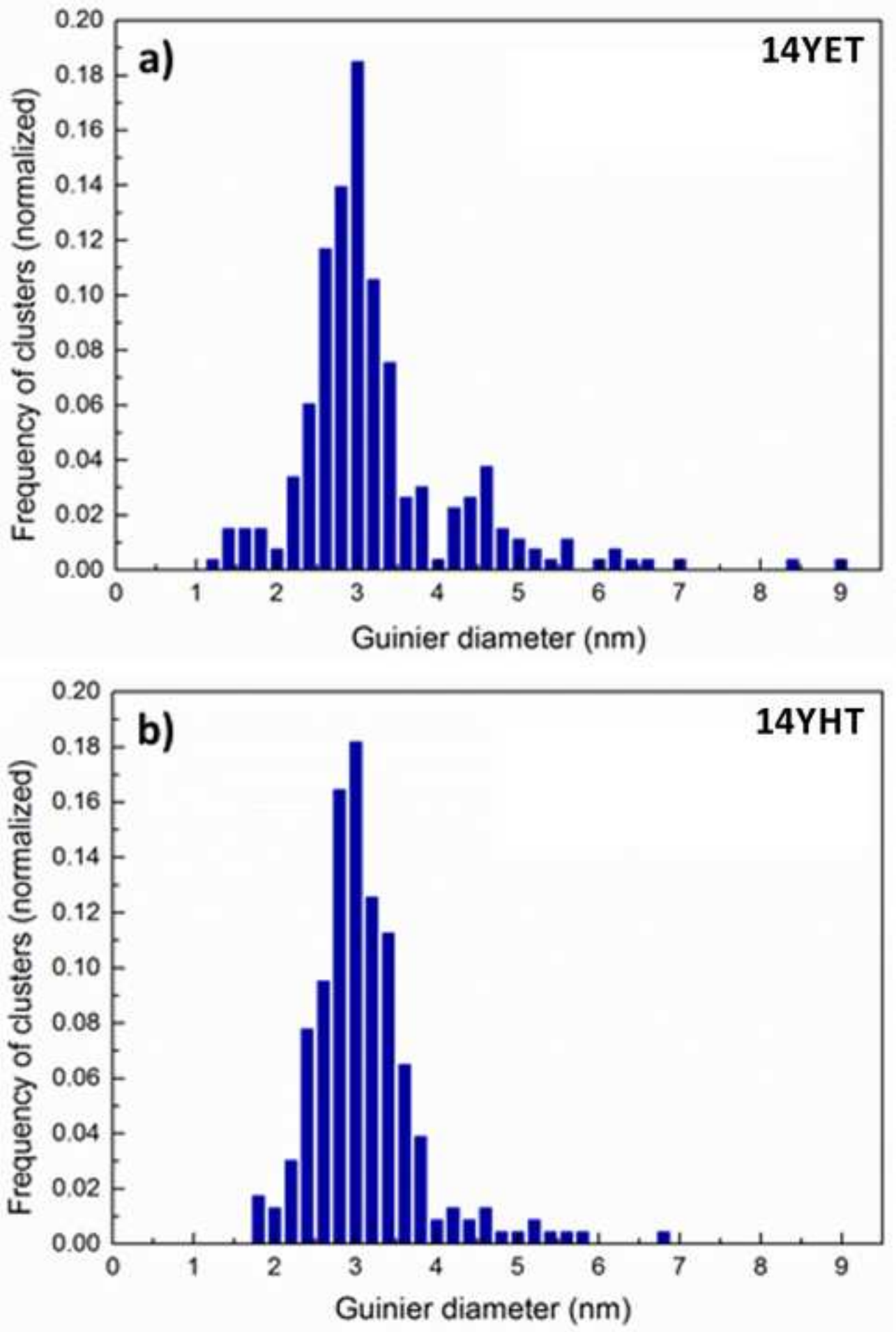

Figure_7
Click here to download high resolution image

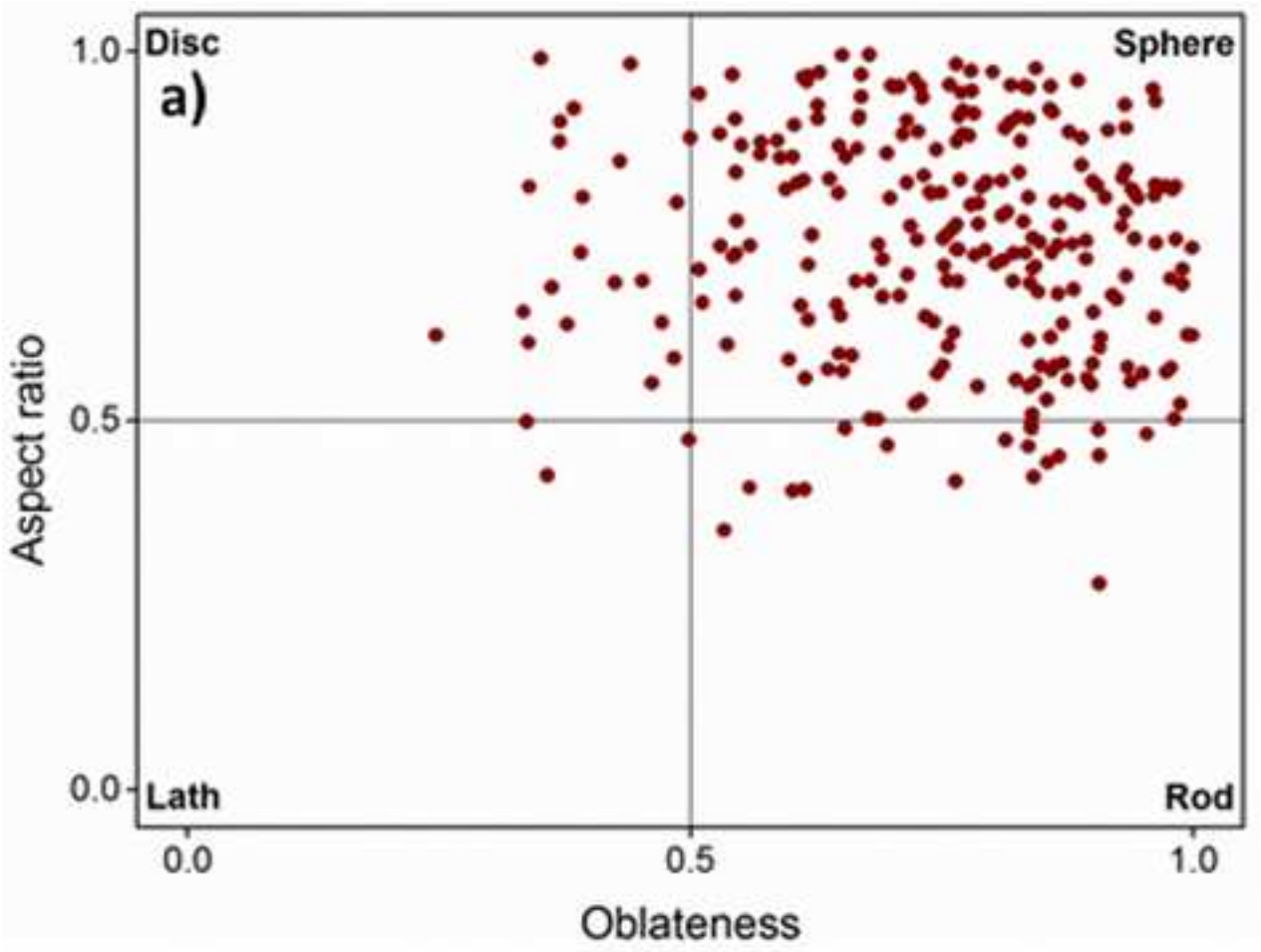

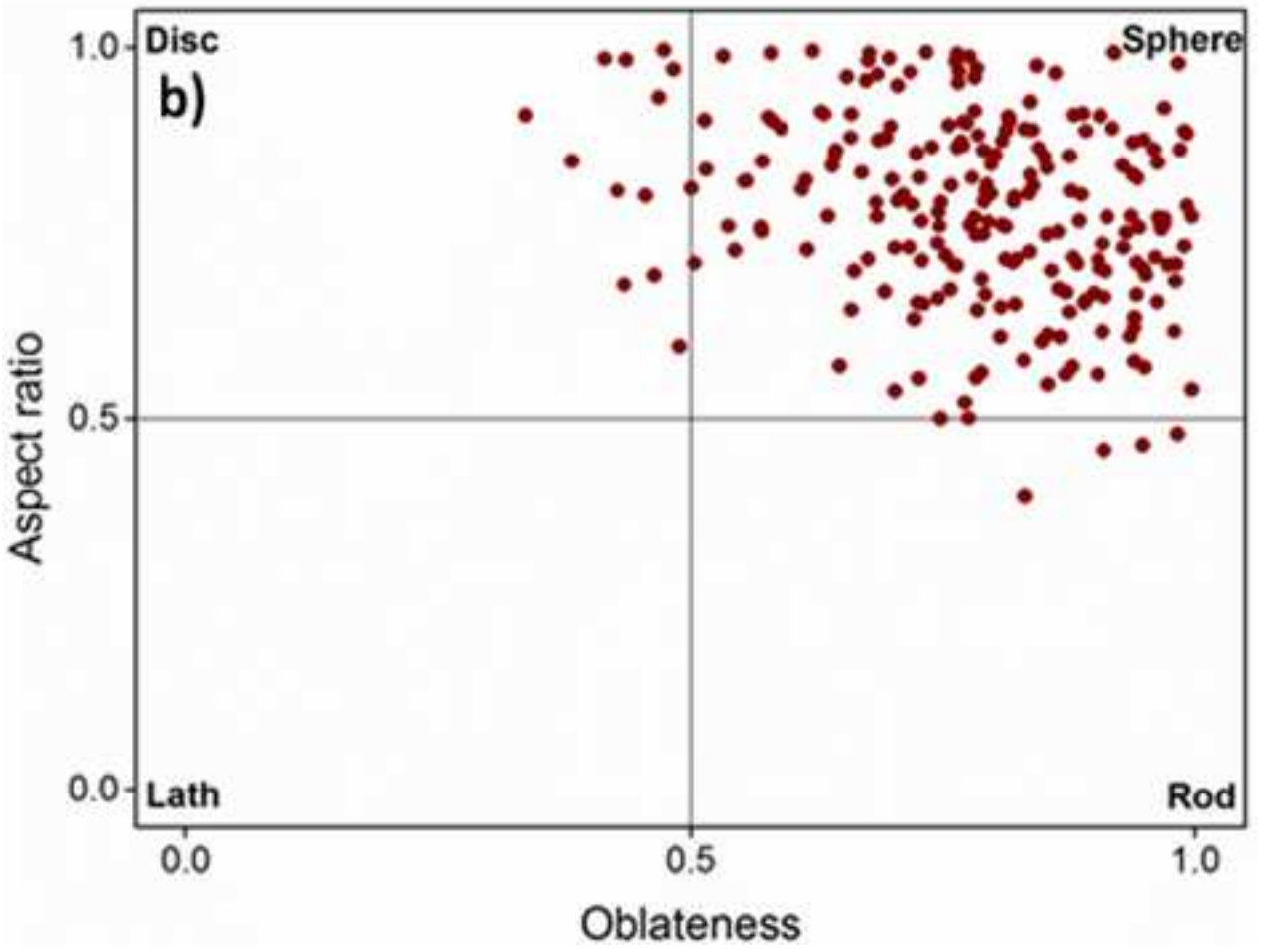

Figure_8

Click here to download high resolution image

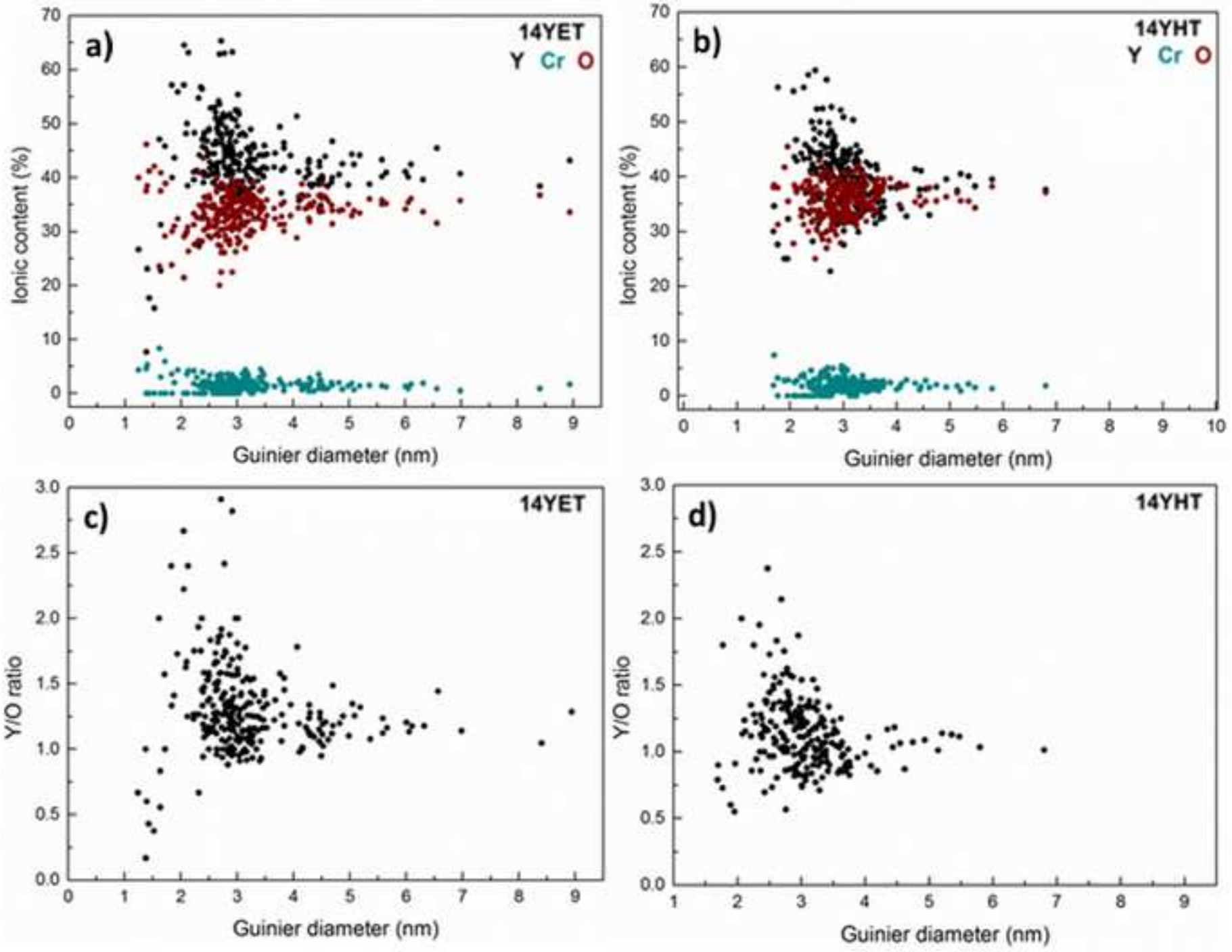

Figure_9
Click here to download high resolution image

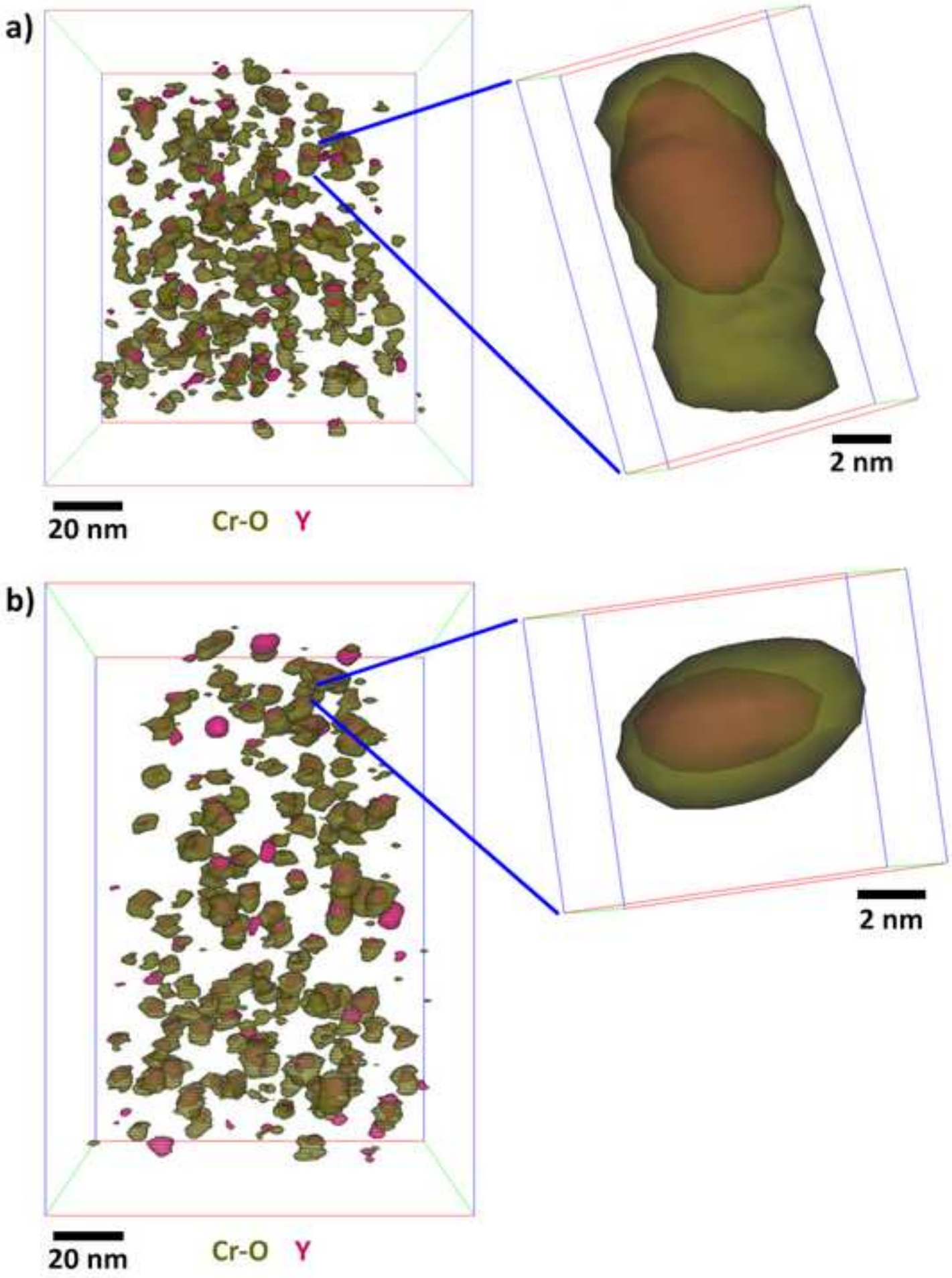

Figure_10
Click here to download high resolution image

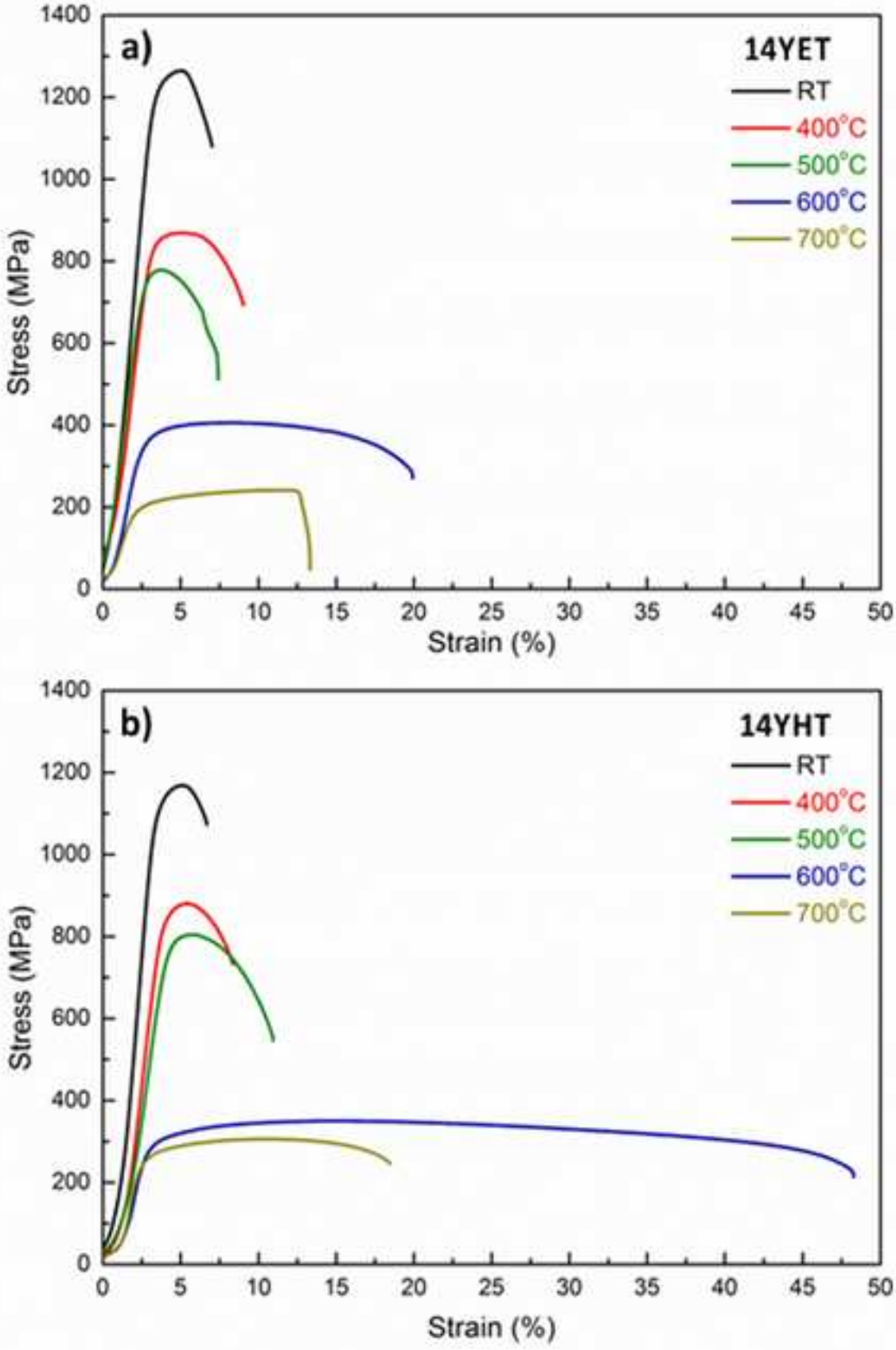

Table(s)

Table I. 14YET and 14YHT average chemical composition in bulk from APT analysis together with the nominal composition.

	Nominal value	**14YET**	**14YHT**
Ion	**(at. %)**	**APT (at. %)**	**APT (at. %)**
Fe	84.76	86.317 ± 0.010	86.064 ± 0.008
Cr	14.87	12.625 ± 0.009	12.751 ± 0.008
Y	0.15	0.101 ± 0.001	0.103 ± 0.001
O	0.22	0.254 ± 0.001	0.306 ± 0.001
C	- - - -	0.007 ± 0.001	0.003 ± 0.000
N	- - - -	0.116 ±0.001	0.093 ± 0.000
Other	- - - -	0.582 ± 0.001	0.681 ± 0.001

Table(s)

Table II. Cluster size summary, number density of clusters and volume fraction of clusters in the 14YET and 14YHT alloys.

	Guinier diameter			**Number density of clusters ($\times 10^{23}$ nm^{-3})**	**Volume fraction of clusters**
	Range (nm)	**Median (nm)**	**Mean value (nm)**		
14YET	1.24 - 8.94	2.94	3.18 ± 1.04	5.7	0.6%
14YHT	1.69 - 6.80	2.98	3.06 ± 0.68	3.3	0.2%

Table(s)

Table III. Cluster shape summary for 14YET and 14YHT alloys.

	Number of analysed clusters	Spherical	Disc shaped	Rod shaped	Lath shaped
14YET	265	84.5%	7.6%	6.8%	1.1%
14YHT	236	93.1%	5.2%	1.7%	0.0%

Table(s)

Table IV. Mechanical properties summary for 14YET and 14YHT alloys, from [10] and [24].

	Yield strength (MPa)		Ultimate tensile strength (MPa)		Uniform elongation (%)		Total elongation (%)	
Temperature	**14YET**	**14YHT**	**14YET**	**14YHT**	**14YET**	**14YHT**	**14YET**	**14YHT**
RT (25°C)	1170	1085	1265	1169	5.0	5.1	7.0	6.7
400°C	805	816	869	880	5.2	5.7	9.0	8.6
500°C	710	751	778	804	3.7	6.6	7.3	11.6
600°C	336	272	407	350	8.3	15.0	19.8	48.1
700°C	176	218	242	294	11.1	8.2	13.3	10.4

Video_1

Click here to download Video: Video_1.mp4

Video_2

Click here to download Video: Video_2.mp4

Video_3

Click here to download Video: Video_3.mp4

Video_4

Click here to download Video: Video_4.mp4

Video_5

Click here to download Video: Video_5.mp4

Video_6

Click here to download Video: Video_6.mp4

Video_7

Click here to download Video: Video_7.mp4

Video_8

Click here to download Video: Video_8.mp4

Video_9

Click here to download Video: Video_9.mp4

Video_10

Click here to download Video: Video_10.mp4